

CrossMark  
click for updatesCite this: *J. Mater. Chem. C*, 2015, 3,  
1949Received 21st November 2014  
Accepted 31st December 2014

DOI: 10.1039/c4tc02663b

www.rsc.org/MaterialsC

## Charge injection promoted electrohydrodynamic instabilities in poly(3-hexylthiophene) thin films

Zhi Ye, Huina Cui, Xiubao Yang and Feng Qiu\*

We investigate the electrohydrodynamic instabilities in poly(3-hexylthiophene) (P3HT) semiconducting polymer films. In the case that a contact is made between the P3HT film and an anode of a doped silicon wafer, the instabilities quickly grow into micro-column arrays in several minutes. The resultant micro-columns in the P3HT film show spherulitic morphology and the polymer chains in the columns are packed with an "edge on" orientation. Charge injection across a small injection barrier is attributed to the promoted electrohydrodynamic instabilities in the thin film.

### Introduction

The transfer of charge carriers across an organic heterojunction is crucial for organic electronics such as light-emitting diodes (OLEDs) and field-effect transistors (OFETs).<sup>1–3</sup> If a contact is made between an electrode and a semiconducting polymer film, charge may be injected from the electrode into the polymer film across an injection barrier.<sup>4</sup> The magnitude of the injection barrier is mainly determined by the mismatch between the energy levels of the polymer semiconductor and the work function of the injecting electrode.<sup>5</sup> It is proven that small injection barriers (*i.e.* lower than 0.4 eV) would facilitate the charge transfer at the electrode/polymer interface and charge injection into semiconducting polymer films could be promoted by reducing the injection barrier.<sup>6,7</sup> The efficiency of charge injection is commonly indicated from the *I–V* characteristics of a device with a sandwich structure.<sup>8</sup> In general, the current density in an *I–V* characteristic reflects the charge transfer rate in the film, which is mainly determined by the two processes of charge injection from the electrode and charge transport across the polymer film.<sup>9,10</sup> Thus the accumulated charge, resulting from charge injection into the polymer film, may be more exact than the measured current density to reflect the efficiency of charge injection when the charge transport process is absent. However, few studies have investigated charge injection with accumulated charge in polymer films. It is still necessary to develop a more effective strategy to detect the net charge within a polymer film and understand charge injection into semiconducting polymer films.

Electrostatic capacitances are suitable for investigating the accumulated charge in polymer films due to the small leakage current and the steady electrostatic field within them.<sup>11,12</sup>

Importantly, the injected charge could accumulate in a semiconducting polymer film without transferring across the film in an electrostatic capacitance.<sup>13,14</sup> In recent years electrostatic capacitances are used in electrohydrodynamic instabilities to pattern polymer films, since it permits a precise control of the destabilizing force over the polymer films by varying the strength and directions of electric fields.<sup>15–17</sup> The evolution of electrohydrodynamic instabilities in polymer films could be used to deduce the polymer properties such as residual stress and nonequilibrium chain conformations, which are hard to be probed by other methods.<sup>18,19</sup> Studies of electrohydrodynamic instabilities mostly involve dielectric liquid of polymers, but few studies have discussed the case of electrohydrodynamic instabilities in conjugated polymers, which commonly belong to a kind of organic semiconductors.<sup>20–22</sup> A possible reason is that conjugated polymers are easy to degrade when being exposed to strong electric fields, leading to no feature of film instability emerging.<sup>23</sup> Actually, the electrohydrodynamic instabilities in a conjugated polymer film are of more importance because the patterning films of conjugated polymers may be applied in various organic electronics.<sup>24</sup> The electrohydrodynamic instabilities in the polymer film are influenced by the polymer conductivity due to the absence of the electric field inside the conductive film,<sup>22,25,26</sup> and thus accumulated charge in the polymer film is possible to be probed by the evolution of the destabilized structures.

Poly(3-hexylthiophene) (P3HT), a typical kind of conjugated polymers, is widely applied in various electronics for its excellent chemical stability and high performance.<sup>27,28</sup> In this work, we develop the strategy of employing electrohydrodynamic instabilities to reveal the charge injection and accumulation in a P3HT film. In contrast to most previous reports involving a relatively weak electric field on conjugated polymers, we study electrohydrodynamic instabilities in the P3HT film by using strong electric fields (*i.e.* 60 V  $\mu\text{m}^{-1}$ ). For the case of the organic/electrode interface at the anode, destabilized structures of

State Key Laboratory of Molecular Engineering of Polymers, and Department of Macromolecular Science, Fudan University, Shanghai 200433, China. E-mail: fengqiu@fudan.edu.cn

column arrays form in a short period of time. The mechanism for the accelerated rate of column growth is investigated. Moreover, we discuss charge injection into semiconducting polymer films with different kinds of injection barriers. The effect of polymer crystallinity on the instability in P3HT films is also discussed.

## Results and discussion

### Electrohydrodynamic instabilities in P3HT films

A P3HT thin film was spin-coated on a highly doped Si wafer, served as a positive electrode with a height stage of 200 nm. The film was covered with a Si/SiO<sub>2</sub> wafer, leaving an air gap, which was created by the height stage. The SiO<sub>2</sub> layer was grown as an insulating layer for reducing the leakage current and increasing the breakdown voltage of a capacitor-like device. The breakdown voltage of the capacitor was detected by a current meter. When a voltage lower than the breakdown voltage is applied on the polymer film, the electric field on the polymer film  $E_p$  and on the SiO<sub>2</sub> layer  $E_{SiO_2}$  are given as  $E_p = U\varepsilon_{SiO_2}\varepsilon_{air}/(h\varepsilon_{SiO_2}\varepsilon_{air} + h_{SiO_2}\varepsilon_p\varepsilon_{air} + h_{air}\varepsilon_p\varepsilon_{SiO_2})$  and  $E_{SiO_2} = U\varepsilon_p\varepsilon_{air}/(h\varepsilon_{SiO_2}\varepsilon_{air} + h_{SiO_2}\varepsilon_p\varepsilon_{air} + h_{air}\varepsilon_p\varepsilon_{SiO_2})$ , where  $U$  is the applied voltage.  $h$ ,  $h_{SiO_2}$  and  $h_{air}$  are the thicknesses of the polymer film, the SiO<sub>2</sub> layer, and the air layer, respectively.  $\varepsilon_p$ ,  $\varepsilon_{SiO_2}$  and  $\varepsilon_{air}$  are the corresponding dielectric constants of polymer, SiO<sub>2</sub> and air. With the instability in the polymer film, the strength of  $E_p$  would fluctuate due to the variation of the dielectric layer thicknesses. According to the equations above, the strength of  $E_p$  would be doubled after the columns span across the two parallel electrodes. SiO<sub>2</sub> has a high dielectric breakdown strength with the theoretical maximum up to  $10^3$  V  $\mu\text{m}^{-1}$ .<sup>29</sup> Therefore, employing a SiO<sub>2</sub> layer inside the capacitor would result in a high breakdown voltage for the device. The breakdown strength of the device was detected by its leakage current, which would increase by several orders of magnitude when the applied electric field reached the breakdown strength of the device. Due to the chemical defects of the thermally grown SiO<sub>2</sub> layer, the breakdown strength of the device was measured in the range of 100–150 V  $\mu\text{m}^{-1}$  on the

P3HT layer. The schematic of electrohydrodynamic instabilities in P3HT films is shown in Fig. 1. When an electric field is applied on the device, electrostatic pressure is created at the polymer/air interface due to capacitor energy minimization and the polymer thin film is destabilized into columns spanning across the parallel electrodes.<sup>30</sup>

**Morphologies.** In the absence of an applied electric field, the 200 °C annealed P3HT film exhibited a featureless morphology, judging from its optical microscope image (Fig. 2a). However, when an electric field of 60 V  $\mu\text{m}^{-1}$  was applied on the film for 5 minutes, a patterned film was obtained, as evidenced by the column arrays of the film (Fig. 2b). The characteristic center-to-center distance between the neighboring columns,  $\lambda$ , was measured to be about 4.1  $\mu\text{m}$ . As the electric-field-annealing time was prolonged to 2 hours, the contrast between the dark dots and the surroundings was enhanced (Fig. 2c). Scanning electron microscopy (SEM) provides a further evidence for the formation of P3HT columns. As shown in Fig. 2d, each column has a flat top with a round shape and the columns are homogeneously distributed on the substrate. These images clearly demonstrate electric fields that are able to generate well-ordered structures on P3HT films over a large area.

We have investigated the surface fluctuations of the P3HT films which were exposed to the electric field for different duration times. In order to minimize the influence of the environment, such as temperature fluctuations, an assembly containing four capacitors was built, with four positive electrodes and a shared negative electrode. Each positive electrode with a P3HT film was removed from the hot stage after being exposed to the electric field for the duration of 1, 2, and 5 minutes, respectively. Atomic force microscopy (AFM) is an excellent tool for observing the nanostructures in the P3HT films because an AFM image can provide nanoscale fluctuations of three-dimensional morphologies. Fig. 3 presents the three-

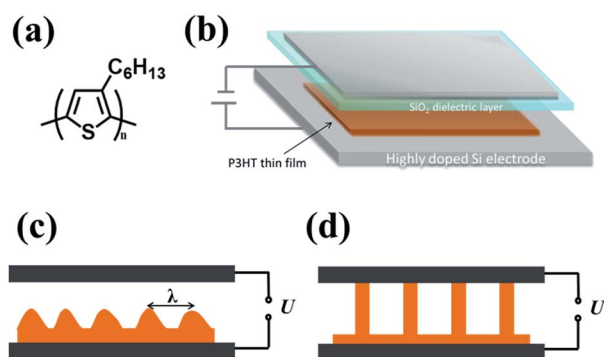


Fig. 1 Schematic of electrohydrodynamic instabilities in P3HT films. (a) Molecular structure of P3HT. (b) Capacitor-like device for a P3HT film under an electric field. A film layer, an air layer and a 200 nm thick SiO<sub>2</sub> layer are included in the device. (c) and (d) The instability evolution in a polymer film in the early and final stages, respectively.

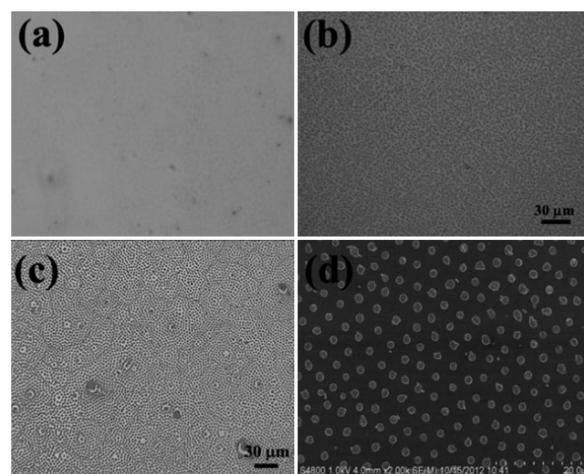


Fig. 2 Micrographs of a P3HT film before and after being applied an electric field. (a) The film was heated to 200 °C and no structure is visible from the optical microscope. (b) and (c) show the optical microscope images with the film exposed to the electric field for 5 minutes and 2 hours, respectively. (d) SEM image of the P3HT column arrays.

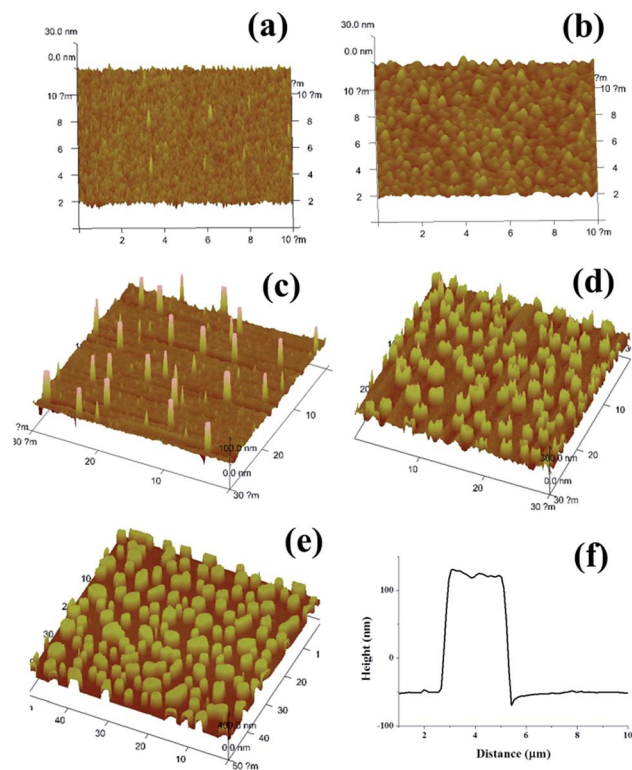


Fig. 3 Morphological evolution of P3HT films under an electric field of  $60 \text{ V } \mu\text{m}^{-1}$ . (a) Typical 3D view of AFM height images for the thermally annealed film for 1 min without any electric field. (b), (c), (d) and (e) are the 3D AFM images of P3HT films treated by the electric field for 1 min, 2 min, 5 min, and 2 h, respectively. (f) is the corresponding cross-sectional line profile in (e).

dimensional AFM images of the P3HT film at the different stages of evolution. The amplitude of the surface fluctuations increases with the electric-field-annealing time. When a P3HT film was treated by thermal annealing without any electric field, the film surface looked rather flat with a roughness of  $\sim 1 \text{ nm}$  according to its AFM height image (Fig. 3a). When an electric field of  $60 \text{ V } \mu\text{m}^{-1}$  was applied on the P3HT film, the surface fluctuations in the film were observed. Fig. 3b shows the early stage of the evolution and a raised pattern with a small undulation appeared on the film. For the P3HT film exposed to an electric field for 1 min, the characteristic distance between the adjacent wave peaks was measured as about  $300 \text{ nm}$  and the average amplitude of the fluctuations was about  $7 \text{ nm}$ . As the electric-field-annealing time was increased to 2 min, the selected growth of the waves was observed, as evidenced by the sparse columns with greater heights, leading to the hierarchical structures in the film (Fig. 3c). The P3HT column arrays were visible after the film was exposed to the electric field for 5 min, as shown in Fig. 3d. Eventually, the P3HT columns stopped growing once they were in contact with the top electrode, and formed a column array that spanned from the substrate electrode to the top electrode. Fig. 3e shows the AFM image of the P3HT film that was exposed to the electric field for 2 h. Fig. 3f is the cross-sectional line profile of a column taken from Fig. 3e and the height of the columns is about  $170 \text{ nm}$ , which is

comparable to the distance of the air gap between the two parallel electrodes.

The growth of the P3HT column arrays takes only several minutes, which are much shorter than the period it would take in dielectric polymer films with a similar value of viscosity.<sup>21,31</sup> During the process of column formation, typical wave-like patterns for the dielectric polymers were not observed, suggesting an unusual process of electrohydrodynamic instabilities in the P3HT films.<sup>32</sup> As far as we know, such column arrays of P3HT have not ever been successfully prepared by utilizing electrohydrodynamic instabilities. In fact, in our experimental conditions, it is the employment of the  $\text{SiO}_2$  layer that largely reduces the leakage current, which stabilizes the P3HT conjugated polymer even in a strong electric field.

**Crystallinity and chain packing.** Polarized optical microscopy (POM) was used to reveal the crystallinity of the P3HT column arrays. The thermally annealed film did not show any Maltase cross patterns in the POM when the polarizers were crossed, due to the very high nucleation density in P3HT films induced by thermal annealing.<sup>33</sup> For the film treated by the electric field for 2 hours, bright column arrays were visible and

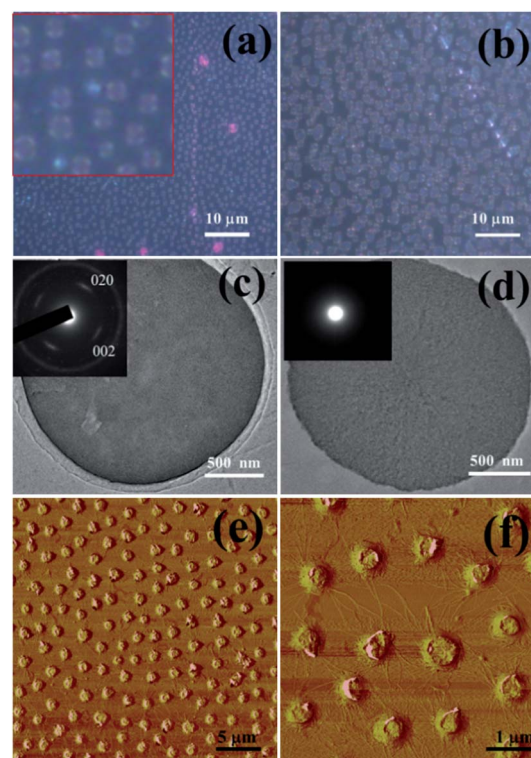


Fig. 4 POM and TEM images of P3HT crystalline columns created by electrohydrodynamic instabilities. POM images of P3HT films treated by the electric field of  $60 \text{ V } \mu\text{m}^{-1}$  (a) and  $90 \text{ V } \mu\text{m}^{-1}$  (b). The inset in (a) is the enlarged image and Maltase cross patterns are visible in the image. TEM images of the circular cross-section from the columns treated by the electric field of  $60 \text{ V } \mu\text{m}^{-1}$  for 2 hours (c) and 5 minutes (d). The insets at the top left corner of (c) and (d) are the corresponding SAED patterns. (e) and (f) are AFM phase images of the P3HT film. The film was treated by the electric field of  $60 \text{ V } \mu\text{m}^{-1}$  for 30 min. The columns are surrounded by wire-like structures, which align their long axis toward the center of the column. The phase scale of the images is  $70^\circ$ .

each column showed a typical Maltase cross pattern (Fig. 4a), indicating the formation of well defined spherulites. The presence of micro-scale spherulites suggests that the electric field is able to reduce the nucleation density in the P3HT film. The increase of the electric field strength also promoted the average diameter of the spherulites. Fig. 4b shows the POM image of a P3HT film exposed to the electric field of  $90 \text{ V } \mu\text{m}^{-1}$ . The P3HT spherulites are larger in diameter than those in Fig. 4a (electric field of  $60 \text{ V } \mu\text{m}^{-1}$ ). A weaker electric field (*i.e.*  $10 \text{ V } \mu\text{m}^{-1}$ ) was also possible to induce the column formation, but much less ordered arrays of P3HT columns were obtained according our experiments.

Since the crystalline columns were evident in the POM images, the polymer packing orientation within the columns was further measured by transmission electron microscopy (TEM) using selected area electron diffraction (SAED). Fig. 4c shows a typical TEM image of the columns taken from the sample treated by the electric field of  $60 \text{ V } \mu\text{m}^{-1}$  for 2 hours. The smooth top of the columns indicates the absence of crystalline lamellae within the columns, which is different from the microstructure in spherulites obtained by the vapor or solvent swelling method.<sup>33</sup> However, lamellae structures were found at the surrounding of the columns in the AFM phase images of the film (Fig. 4e and f). The diffraction pattern in the inset of Fig. 4c identifies a typical “edge on” orientation of the P3HT chains within the crystalline columns, as evidenced by the presence of (020) and (002) diffractions, corresponding to the  $\pi$ - $\pi$  stacking distance and the periodic length along the backbone direction of P3HT, respectively. Fig. 4d shows a typical TEM image taken on the columns from the electric-field-annealed sample for 5 min. The absence of diffraction rings indicates that the P3HT columns are in amorphous form or with a very low degree of crystallinity (Fig. 4d). Thus it is reasonable to deduce that the column crystallization of P3HT is followed by the column formation. Interestingly, the column spherulites were observed only in the case of the organic/electrode interface at the anode under electric fields. If the resultant amorphous columns (*i.e.* Fig. 3d) were only treated by thermal annealing, no column spherulites were observed from their POM images. This indicates that net charge in the P3HT film may play a significant role in the formation of polymer spherulites.

SAED measurements only determine the local arrangement of the polymer chains within the P3HT columns. To further investigate the crystallinity and molecular packing orientation over the whole film, synchrotron X-ray grazing incidence diffraction (GIXRD) was performed for the P3HT film with column arrays. Fig. 5a presents a 2D GIXRD image of the P3HT film, which was annealed in the electric field for 5 min and destabilized with column arrays. A faint diffraction point corresponding to the (100) lamellar distance of P3HT was recorded, reflecting the low degree of crystallinity of the P3HT film. The results coincide well with the SAED measurements, which prove that the columns are amorphous in the early stage of the column formation. When the electric-field-annealing time was increased to 2 hours, the (100) diffraction point in the GIXRD image became much brighter, as shown in Fig. 5b. The presence of (100) diffraction in the  $Q_z$  direction indicates the “edge on” orientation of the molecular packing over the whole film.

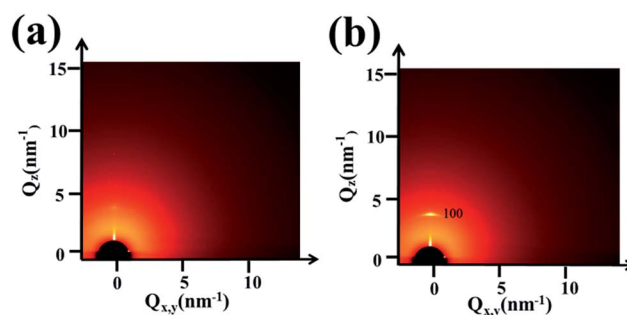


Fig. 5 2D GIXRD images for the P3HT films with column patterns. P3HT thin films have been treated by the electric field for 5 minutes (a) and 2 hours (b), respectively.

Another case of the organic/electrode interface at the cathode was considered. The setup was similar to the previous capacitor except for the electrode connections, where the Si wafer with the P3HT film was connected to the negative source. When the film was heated to  $200 \text{ }^\circ\text{C}$ , in its AFM height image, the pattern was featureless (Fig. 6a). Fig. 6b and c depict the AFM images and the corresponding OM images of the P3HT thin films after being exposed to an electric field for 8 hours. The wave-like pattern was similar to the pattern observed in a dielectric polymer fluid under electric fields, indicating that in this case the semiconducting P3HT behaved like a dielectric polymer.<sup>32</sup> The characteristic distance was measured to be  $5\text{--}10 \text{ } \mu\text{m}$  and the wave-like pattern included various destabilized structures at different stages of wave growth. As shown in Fig. 6d, the waves in the right part of the image seem to be destabilized well compared to that in the left part of the image. As time progressed, in the P3HT film deeper waves or column

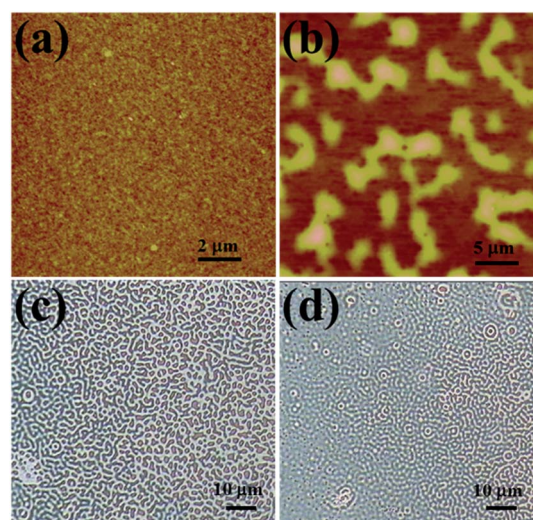


Fig. 6 Wave-like pattern in the P3HT film induced by electric fields. (a) AFM image of the thermal-annealed film without electric fields. (b) AFM image of the electric-field-annealed film. The P3HT film was exposed to  $60 \text{ V } \mu\text{m}^{-1}$  electric field at  $200 \text{ }^\circ\text{C}$  for 8 hours. The height scale of the images is  $20 \text{ nm}$ . (c) and (d) corresponding optical images of (b). The characteristic distance is measured to be  $5\text{--}10 \text{ } \mu\text{m}$ .

structures were not formed under electric fields. The presence of various destabilized structures in the same film may reflect that P3HT do not crystallize simultaneously at different places in the P3HT film. The effect of P3HT crystallization on the instability process will be explained in the following discussion.

Fig. 7 plots the roughness of the P3HT film as a function of the electric-field-annealing time for the two cases of electrode connection. The film roughness is represented by the root-mean-square height of the patterns in the AFM images. Obviously, for the case that the Si wafer covered with the P3HT film was connected to the positive source, the P3HT film was easily destabilized, leading to a much rougher surface. A dramatic increase of the film roughness was observed when it was annealed under the electric field within 5 minutes, see Fig. 7 (red line). For the other case of the organic/electrode interface at the cathode, the fluctuations in the film were much smaller, with a roughness of about 10 nm (black line). One possible explanation for this is that the electric field direction is different between the two cases. Interestingly, according to the dispersion relation for dielectric polymers, the applied electric field directions seem not to affect the instability process of a dielectric polymer fluid.<sup>30,34</sup>

Another possible explanation is the charge type difference at the organic/electrode interface between the two cases of electrode connection. When a contact is made at an electrode/semiconductor interface, charge injection with holes or electrons may take place from the electrode to the semiconductor film.<sup>7</sup> To confirm this supposition, a comparative curve is given in Fig. 7. The experimental conditions with the blue curve were the same as with the red curve, except that a SiO<sub>2</sub> layer was inserted between the P3HT film and the Si electrode at the anode. However, it is clear that the blue curve is more close to the black curve. The results suggest that it is not the electric field direction but the contact at the polymer/electrode interface that plays a significant role in promoting electrohydrodynamic

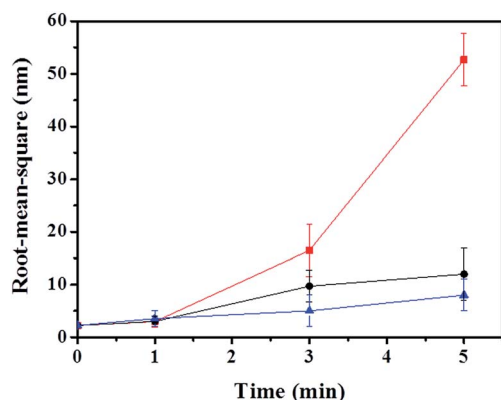


Fig. 7 Roughness of the P3HT films as a function of the electric-field-annealing time. The roughness (root-mean-square) of the films are obtained from the corresponding AFM height images. The red and black curves represent the two cases of the organic/electrode interface at the anode and cathode, respectively. The blue curve represents the same experimental conditions as the red curve, except that a SiO<sub>2</sub> layer was inserted between the P3HT film and the Si electrode at the anode.

instabilities in P3HT films. Whether charge carriers are easily injected into organic semiconductor films mainly depends on the magnitude of the injection energy barrier.<sup>5</sup> The hole- and electron-injection energetic barriers  $\Delta$  are mostly determined by the difference between the work function (WF) of the electrodes and the highest occupied molecular orbital (HOMO), and the difference between the WF of the electrodes and the lowest unoccupied molecular orbital (LUMO) of polymer semiconductors.<sup>35</sup> In the presence of an electric field, the energy barrier  $\Delta_\phi$  is predicted to follow:<sup>36,37</sup>  $\Delta_\phi = \Delta - \left( \frac{e^3 E}{4\pi\epsilon_p\epsilon_0} \right)^{0.5}$ ,

where  $E$  is the applied electric field on the semiconducting film,  $e$  is the unit charge,  $\epsilon_p$  is the relative dielectric constant of organic semiconductors,<sup>38</sup>  $\epsilon_0$  is the vacuum permittivity. P3HT has a HOMO energy level of  $-5.1$  eV and a LUMO of  $-3.1$  eV.<sup>39</sup> The WF of the highly n-doped silicon electrode is estimated to be  $4.85$  eV.<sup>40</sup> The bending energy level caused by the electric field is  $\sim 0.1$  eV on the basis of the second term  $\left( \frac{e^3 E}{4\pi\epsilon_p\epsilon_0} \right)^{0.5}$ .<sup>37,41</sup>

So the injection barrier for the hole injection is calculated as  $0.15$  eV, which is several times higher than  $0.04$  eV of thermal fluctuations ( $kT$ ). For the case of the organic/electrode interface at the cathode, electrons from the cathode may be injected into the LUMO of the organic semiconductor, depending on the magnitude of the injection barrier.<sup>6,42</sup> According to the equation above, the injection barrier from the Si electrode to the P3HT film is calculated to be  $1.65$  eV, which is too large for electron injection from the electrode to the polymer film efficiently.<sup>43,44</sup>

Daivids *et al.* have found the charges were easily injected from the electrode when the injection barrier was less than  $0.4$  eV, judging from the  $I$ - $V$  characteristics *via* a diode-like device.<sup>6</sup> In the device, the detected current density reflects the charge transfer rate across the film, which is affected by both the processes of charge injection and transfer.<sup>5,9,10</sup> In our experiments, charge transfer across the film is hindered by the air/SiO<sub>2</sub> layer, thus the accumulated charge in the P3HT film is more exact to reflect the efficiency of charge injection from the electrode.

The accumulated charge in a film owing to charge injection may be revealed by the destabilizing rate of the P3HT film under electric fields. The net charge in polymer films are believed to have an impact on the electrostatic pressure at the polymer/air interface, and thus accelerate the growth of film instabilities.<sup>25</sup> The capacitor with a charged film has a capacitor energy  $W$  and an electrostatic pressure  $P_{el}$  at the film/air interface:

$$W = 1/2\epsilon_0 S \frac{1}{d-h} U^2, P_{el} = \frac{1}{S} \partial W / \partial h = -\frac{1}{2} \epsilon_0 \frac{U^2}{(d-h)^2}, \text{ where } \epsilon_0$$

is the dielectric permittivity of the vacuum,  $U$  is the applied voltage on the device,  $d$  is the distance between the two parallel electrodes, and  $h$  is the film thickness.  $\tau^{-1}$  is the growth rate, expressed as in the equation:<sup>34</sup>

$$\tau^{-1} = -\frac{h^3}{3\eta} \left( \gamma q^4 + \frac{\partial P_{el}}{\partial h} q^2 \right) = -\frac{h^3}{3\eta} \left( \gamma q^4 - \epsilon_0 \frac{U^2}{(d-h)^3} q^2 \right).$$

When the surface undulation is created by an electric field, the film thickness  $h$  at different positions  $x$  changes with time  $t$ ,

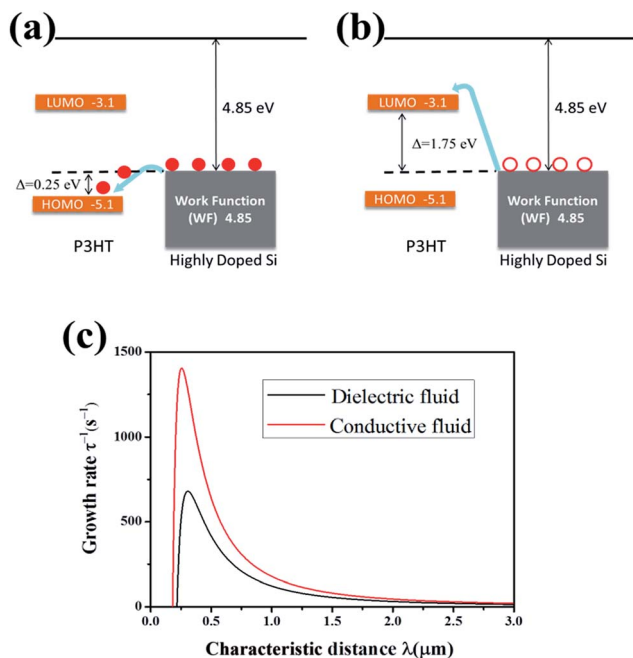


Fig. 8 Energy levels of charge injection for positive electrode connection (a) and negative electrode connection (b) from doped Si electrode into P3HT. The filled circulars are positive charge (holes) and hollow circulars are negative charge (electrons). (c) Prediction of the growth rate with  $\lambda$  for a conductive film (red curve) and a dielectric film (black curve).

represented by  $h(x, t)$ .  $q$  is the wavenumber of a small undulation.  $\gamma$  is the surface tension ( $18 \text{ mN m}^{-1}$  for P3HT melt) and  $\eta$  is the polymer viscosity ( $99 \text{ Pa s}$  for P3HT melt).<sup>45,46</sup>  $h$  represents the initial film thickness of  $\sim 40 \text{ nm}$ . Fig. 8 plots the growth rate  $\tau^{-1}$  as a function of characteristic distance  $\lambda$  in the electric field of  $60 \text{ V } \mu\text{m}^{-1}$ . The maximum growth rate is calculated to be  $1405 \text{ s}^{-1}$  when the charge is injected into the polymer film. In the case of a perfect dielectric of a polymer film, the growth rate could be predicted using a linear stability analysis, which is given by:<sup>18</sup>

$$\tau^{-1} = -\frac{h^3}{3\eta} \left( \gamma q^4 - \frac{[\epsilon_0 \epsilon_p (\epsilon_p - 1) E_p]^2}{\partial h} q^2 \right). \text{ Thus the maximum}$$

growth rate is  $681 \text{ s}^{-1}$  with the same applied voltage. The predictions indicate that the charge injection can play a significant role in promoting the growth of the waves in the early stage of destabilization. According to the equation above, the growth rate is inversely proportional to the film viscosity  $\eta$  which would increase with the polymer crystallinity.<sup>47,48</sup> As a typical semicrystalline material, P3HTs tend to crystallize within the range of crystallization temperatures.<sup>49</sup> Thus the growth rate of the instabilities in P3HT films would decrease with time at the crystallization temperature of P3HT. According to the diffraction results in Fig. 4 and 5, the crystallinity of the P3HT film remains low after the electrical-field annealing for 5 minutes. Therefore, if the instability-growing process could finish in a short period of time, the influence of polymer crystallization would be minimized. In this case the polymer crystallization may enlarge the difference of the resultant patterns between a charged film and an electrically neutral film.

## Conclusions

In summary, we have explored the use of electrohydrodynamic instabilities in P3HT films for detecting the charge injection in the polymer semiconductor film. Different from the dielectric polymer films, the P3HT film seems easy to be destabilized by electric fields, leading to column patterns in the case of the organic/electrode interface at the anode. The roughness of the P3HT film increases substantially from  $2.7 \text{ nm}$  to  $52.7 \text{ nm}$  under the electric field on the time scale of 5 min. However, when the organic/electrode interface is switched to the cathode or inserted with an insulating layer, the increase of roughness is small for the same period of annealing time. On the basis of the predictions about the electrohydrodynamic instabilities in P3HT films with net charge, charge injection from the anode is believed to take place in the case of a small injection barrier of  $0.15 \text{ eV}$  and thus promotes the instabilities in P3HT films. If the injection barrier increases to  $1.65 \text{ eV}$ , charge carriers are found hard to transfer across the contact. SAED experiments combined with GIXRD measurements prove that the column array formation is followed by the crystallization of P3HT. The resultant micrometer-scale spherulitic columns of P3HT provide the evidence that the electrohydrodynamic instabilities in charged P3HT films may reduce the nucleation density in the films. Inducing electrohydrodynamic instabilities in semiconducting polymer films may become a simple and effective strategy to study charge injection into conjugated polymer films and generate patterns of polymer semiconductors over large areas.

## Experimental section

### Materials

Highly doped n-type Si substrates, conductive silver glues and copper lines were purchased from Materials Technology Company. The insulating layer of  $\text{SiO}_2$  was grown on the Si wafer *via* dry-oxygen oxidation method, resulting in a low density of chemical defects within the  $\text{SiO}_2$  layer. The thickness of the  $\text{SiO}_2$  layer was measured as  $200 \pm 25 \text{ nm}$ . Regioregular poly(3-hexylthiophene) (P3HT) ( $M_n = 11 \text{ kg mol}^{-1}$ , 98% regioregularity) was synthesized by a modified Grignard Metathesis procedure in our lab.  $200 \text{ nm}$  diameter  $\text{SiO}_2$  balls, chloroform, hydrofluoric acid, toluene, and octadecyltrichlorosilane (ODTS) were purchased from Sigma-Aldrich. Toluene was distilled from sodium/benzophenone and all the others were used as received.

### Experimental setup

A height stage of  $\sim 200 \text{ nm}$  on the Si substrate was created by etching the center part of the  $\text{SiO}_2$  layer or by dispersing  $\text{SiO}_2$  balls on the Si wafer. The wafers were pre-cleaned with acetone, isopropyl alcohol and de-ionized water in succession and dried by  $\text{N}_2$  snow-jet. Then they were pre-cleaned with  $\text{H}_2\text{SO}_4/\text{H}_2\text{O}_2$  (3 : 1 in volume) solution and de-ionized water. The native oxide layers on the Si wafers were removed by hydrofluoric acid. P3HT was dissolved in chloroform solution and heated on a hot stage at  $90 \text{ }^\circ\text{C}$  in a sealed vial. The P3HT solution ( $10 \text{ mg ml}^{-1}$ ) was

filtered with a 0.22  $\mu\text{m}$  PTFE filter before cooling down to room temperature. P3HT thin films were prepared on the Si substrate by the spin coating process at 3000 rpm. The spin-coated film had a thickness of  $40 \pm 10$  nm, which was measured by an atomic force microscope (AFM). The  $\text{SiO}_2/\text{Si}$  was modified by an ODTs layer to reduce the interactions between P3HT columns and the  $\text{SiO}_2$  layer. The upper electrode of the  $\text{SiO}_2/\text{Si}$  wafer was covered on the film, forming a capacitor-like device, which consisted of two parallel electrodes and a small air gap of 200 nm between the two plates. The assembly was fixed by a home-made brace on a hot stage, which was used to heat the P3HT film above its glass transition temperature. The bottom and top electrodes were connected to two copper lines respectively *via* conductive silver glues. Then the copper lines were connected to a DC voltage source (Keithley 2400), which provides an electrostatic field to the device. The leakage current in the device was measured with the digital meter with the purpose of monitoring the fluctuation of electric field strength and determining the breakdown voltage of the device. For high temperature experiments, the assembly was placed in a glove box in order to prevent the P3HT film from oxidation by  $\text{O}_2$ .

### Characterization

The morphologies in P3HT films were characterized by AFM (Bruker Multimode Nanoscope IV) with tapping mode. The polarized optical microscope (Leica, DM2500P) was used to observe the P3HT crystallites. For the TEM characterization, the structured film was embedded in epoxy resin. After being solidified in an oven at 60  $^\circ\text{C}$  for 48 h, the epoxy resin was peeled from the Si substrate and was sliced using an ultramicrotome, yielding circular crosssections of columns with a thicknesses smaller than 100 nm. The TEM and SAED measurements were characterized using a JEOL field-emission transmission electron microscope at the operating voltage of 200 kV. The crystallinity of the P3HT film was studied with the 2D X-ray grazing incidence diffraction (GIXRD) technique, performed at BL14B1 of the Shanghai Synchrotron Radiation Facility. The incidence angle of the X-ray beam line was 0.18 $^\circ$  and the exposure time was 30 seconds in our measurements.

### Acknowledgements

We gratefully acknowledge the financial support from the National Basic Research Program of China (Grant no. 2011CB605700) and the National Natural Science Foundation of China (Grant no. 21320102005). We also gratefully acknowledge the support from the BL14B beamline of the Shanghai Synchrotron Radiation Facility of China for the grazing-incidence X-ray diffraction (GIXRD) experiment.

### Notes and references

- 1 M. C. Gwinner, F. Jakubka, F. Gannott, H. Sirringhaus and J. Zaumseil, *ACS Nano*, 2012, **6**, 539–548.
- 2 R. H. Friend, R. W. Gymer, A. B. Holmes, J. H. Burroughes, R. N. Marks, C. Taliani, D. D. C. Bradley, D. A. Dos Santos,

- J. L. Bredas, M. Logdlund and W. R. Salaneck, *Nature*, 1999, **397**, 121–128.
- 3 K. J. Baeg, J. Kim, D. Khim, M. Caironi, D. Y. Kim, I. K. You, J. R. Quinn, A. Facchetti and Y. Y. Noh, *ACS Appl. Mater. Interfaces*, 2011, **3**, 3205–3214.
- 4 R. Nouchi, M. Shigeno, N. Yamada, T. Nishino, K. Tanigaki and M. Yamaguchi, *Appl. Phys. Lett.*, 2014, **104**, 013308.
- 5 V. I. Arkhipov, E. V. Emelianova, Y. H. Tak and H. Bassler, *J. Appl. Phys.*, 1998, **84**, 848–856.
- 6 P. S. Davids, I. H. Campbell and D. L. Smith, *J. Appl. Phys.*, 1997, **82**, 6319–6325.
- 7 J. C. Scott, *J. Vac. Sci. Technol., A*, 2003, **21**, 521–531.
- 8 R. Valaski, L. M. Moreira, L. Micaroni and I. A. Hummelgen, *J. Appl. Phys.*, 2002, **92**, 2035–2040.
- 9 T. W. Lee, J. J. Park, Y. Kwon, T. Hayakawa, T. L. Choi, J. H. Park, R. R. Das and M. A. Kakimoto, *Langmuir*, 2008, **24**, 12704–12709.
- 10 L. Fradkin, R. E. Palacios, J. C. Bolinger, K. J. Lee, W. M. Lackowski and P. F. Barbara, *J. Phys. Chem. A*, 2009, **113**, 4739–4745.
- 11 S. L. M. van Mensfoort and R. Coehoorn, *Phys. Rev. Lett.*, 2008, **100**, 086802.
- 12 F. L. Liu, P. P. Ruden, I. H. Campbell and D. L. Smith, *Appl. Phys. Lett.*, 2012, **101**, 023501.
- 13 H. Cohen, R. Maoz and J. Sagiv, *Nano Lett.*, 2006, **6**, 2462–2466.
- 14 D. L. John, L. C. Castro and D. L. Pulfrey, *J. Appl. Phys.*, 2004, **96**, 5180–5184.
- 15 E. Schaffer, T. Thurn-Albrecht, T. P. Russell and U. Steiner, *Nature*, 2000, **403**, 874–877.
- 16 Z. Q. Lin, T. Kerle, T. P. Russell, E. Schaffer and U. Steiner, *Macromolecules*, 2002, **35**, 3971–3976.
- 17 P. Goldberg-Oppenheimer, P. Kohn, R. M. Langford and U. Steiner, *Small*, 2012, **8**, 2595–2601.
- 18 D. R. Barbero and U. Steiner, *Phys. Rev. Lett.*, 2009, **102**, 248303.
- 19 K. R. Thomas, A. Chenneviere, G. Reiter and U. Steiner, *Phys. Rev. E: Stat., Nonlinear, Soft Matter Phys.*, 2011, **83**, 021804.
- 20 A. del Campo and E. Arzt, *Chem. Rev.*, 2008, **108**, 911–945.
- 21 N. Wu and W. B. Russel, *Nano Today*, 2009, **4**, 180–192.
- 22 S. Manigandan, S. Majumder, A. Suresh, S. Ganguly, K. Kargupta and D. Banerjee, *Sens. Actuators, B*, 2010, **144**, 170–175.
- 23 F. A. de Castro, F. Nuesch, C. Walder and R. Hany, *J. Nanomater.*, 2012, **2012**, 478296.
- 24 Z. H. Nie and E. Kumacheva, *Nat. Mater.*, 2008, **7**, 277–290.
- 25 P. Gambhire and R. M. Thakkar, *Phys. Rev. E: Stat., Nonlinear, Soft Matter Phys.*, 2012, **86**, 036301.
- 26 L. F. Pease and W. B. Russel, *J. Non-Newtonian Fluid Mech.*, 2002, **102**, 233–250.
- 27 M. He, W. Han, J. Ge, Y. L. Yang, F. Qiu and Z. Q. Lin, *Energy Environ. Sci.*, 2011, **4**, 2894–2902.
- 28 J. Ge, M. He, F. Qiu and Y. L. Yang, *Macromolecules*, 2010, **43**, 6422–6428.
- 29 K. V. Shcheglov, C. M. Yang, K. J. Vahala and H. A. Atwater, *Appl. Phys. Lett.*, 1995, **66**, 745–747.

- 30 Z. Q. Lin, T. Kerle, S. M. Baker, D. A. Hoagland, E. Schaffer, U. Steiner and T. P. Russell, *J. Chem. Phys.*, 2001, **114**, 2377–2381.
- 31 N. E. Voicu, S. Harkema and U. Steiner, *Adv. Funct. Mater.*, 2006, **16**, 926–934.
- 32 K. A. Leach, Z. Q. Lin and T. P. Russell, *Macromolecules*, 2005, **38**, 4868–4873.
- 33 E. J. W. Crossland, K. Rahimi, G. Reiter, U. Steiner and S. Ludwigs, *Adv. Funct. Mater.*, 2011, **21**, 518–524.
- 34 E. Schaffer, T. Thurn-Albrecht, T. P. Russell and U. Steiner, *Europhys. Lett.*, 2001, **53**, 518–524.
- 35 Y. Xu, K. J. Baeg, W. T. Park, A. Cho, E. Y. Choi and Y. Y. Noh, *ACS Appl. Mater. Interfaces*, 2014, **6**, 14493–14499.
- 36 Z. Chiguvare, J. Parisi and V. Dyakonov, *J. Appl. Phys.*, 2003, **94**, 2440–2448.
- 37 P. W. M. Blom and M. C. J. M. Vissenberg, *Mater. Sci. Eng., R*, 2000, **27**, 53–94.
- 38 D. C. Tiwari, V. Sen and R. Sharma, *Indian J. Pure Appl. Phys.*, 2012, **50**, 49–56.
- 39 B. H. Hamadani and D. Natelson, *J. Appl. Phys.*, 2005, **97**, 064508.
- 40 H. B. Michaelson, *J. Appl. Phys.*, 1977, **48**, 4729–4733.
- 41 S. H. Jeong and K. H. Lee, *Semiconductor Nanomaterials for Flexible Technologies*, 2010, p. 132.
- 42 A. Garcia, J. Z. Brzezinski and T. Q. Nguyen, *J. Phys. Chem. C*, 2009, **113**, 2950–2954.
- 43 H. Lee, J. Lee, K. Jeong, Y. Yi, J. H. Lee, J. W. Kim and S. W. Cho, *J. Phys. Chem. C*, 2012, **116**, 13210–13216.
- 44 N. K. Kim, D. Khim, Y. Xu, S. H. Lee, M. Kang, J. Kim, A. Facchetti, Y. Y. Noh and D. Y. Kim, *ACS Appl. Mater. Interfaces*, 2014, **6**, 9614–9621.
- 45 N. P. Holmes, K. B. Burke, P. Sista, M. Barr, H. D. Magurudeniya, M. C. Stefan, A. L. D. Kilcoyne, X. J. Zhou, P. C. Dastoor and W. J. Belcher, *Sol. Energy Mater. Sol. Cells*, 2013, **117**, 437–445.
- 46 Y. Y. Yimer, A. Dhinojwala and M. Tsige, *J. Chem. Phys.*, 2012, **137**, 044703.
- 47 S. Coppola, L. Balzano, E. Gioffredi, P. L. Maffettone and N. Grizzuti, *Polymer*, 2004, **45**, 3249–3256.
- 48 J. Wang and R. S. Porter, *Rheol. Acta*, 1995, **34**, 496–503.
- 49 S. Malik and A. K. Nandi, *J. Polym. Sci., Part B: Polym. Phys.*, 2002, **40**, 2073–2085.